

Comparisons of CME morphological characteristics derived from five 3D reconstruction methods

L. Feng^{1,2} · B. Inhester² · M. Mierla^{3,4}

© Springer ●●●

Abstract

We compare different methods to reconstruct the three-dimensional (3D) CME morphology. The explored methods include geometric localisation, mask fitting, forward modeling, polarisation ratio and local correlation tracking plus triangulation. The five methods are applied to the same CME event, which occurred on August 7 2010. Their corresponding results are presented and compared, especially in their propagation direction and spatial extent in 3D. We find that mask fitting and geometric localisation method produce consistent results. Reconstructions including three-view observations are more precise than reconstructions done with only two views. Compared to the forward modeling method, in which a-priori shape of the CME geometry is assumed, mask fitting has more flexibility. Polarisation ratio method makes use of the Thomson scattering geometry. We find spatially the 3D CME derived from mask fitting lies mostly in the overlap region obtained with the polarisation method from COR2 A and B. In addition, mask fitting can help resolve the front/back ambiguity inherent in the polarisation ratio method. However, local correlation tracking plus triangulation did not show a consistent result with the other four methods. For reconstructions of a diffuse CME, when the separation angle between STEREO A and B is large, finding two corresponding points in a STEREO image pair becomes very difficult. Excluding the local correlation tracking method, the latitude of the CME's centre of gravity derived from the other methods deviates within one degree and longitude differs within 19 degrees.

Keywords: Corona,structures-Coronal mass ejections,initiation and propagation

¹ Key Laboratory of Dark Matter and Space Astronomy, Purple Mountain Observatory, Chinese Academy of Sciences, 210008 Nanjing, China email: lfeng@pmo.ac.cn

² Max-Planck-Institut für Sonnensystemforschung, Max-Planck-Str.2, 37191 Katlenburg-Lindau, Germany email: binhest@mps.mpg.de

³ Institute of Geodynamics of the Romanian Academy Jean-Louis Calderon 19-21, Bucharest-37, Romania, RO-020032 email: marilena@geodin.ro

⁴ Royal Observatory of Belgium, Avenue Circulaire 3, 1180 Brussels, Belgium

1. Introduction

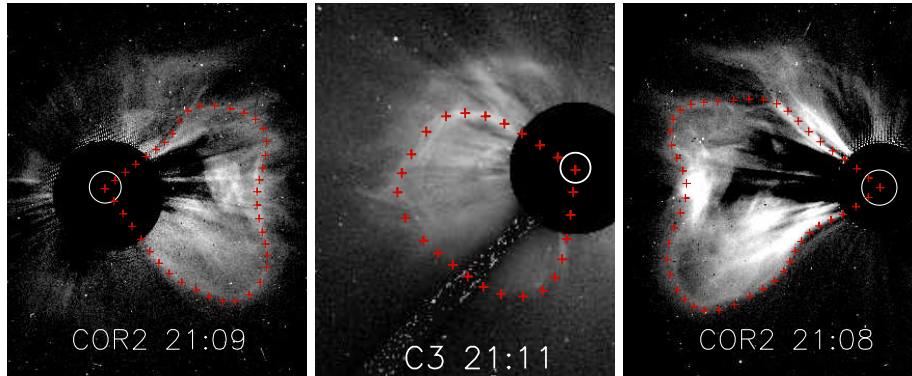
Coronal mass ejections (CMEs) are violent eruptions from the Sun and also known as the main cause of major geomagnetic storms. They can now be observed from three viewpoints almost simultaneously using the two separated Solar Terrestrial Relations Observatory (STEREO) spacecraft (Kaiser *et al.*, 2008) and SOLar and Heliospheric Observatory (SOHO) (Domingo, Fleck, and Poland, 1995). COR 1 & 2 are white-light coronagraphs in the Sun Earth Connection Coronal and Heliospheric Investigation (SECCHI; Howard *et al.* (2008)) instrument package onboard STEREO. Large and Spectroscopic Coronagraph (LASCO; Brueckner *et al.* (1995)) C2 and C3 are white-light coronagraphs onboard SOHO. They provide time-resolved polarised and total brightness images of eruptions in the corona. Such measurements can be used to derive the location and 3D structure of CMEs, which is crucial for understanding the origin and dynamics of these eruptions and for predicting their effects on the Earth's magnetosphere.

A number of methods have been developed to obtain the 3D morphology of CMEs from multi-view coronagraph data. Mierla *et al.* (2009, 2010) and Thernisien, Vourlidas, and Howard (2011) compared the results of different reconstruction methods. de Koning, Pizzo, and Biesecker (2009) calculated a stack of quadrilaterals which contain the 3D CME position and shape. Byrne *et al.* (2010) fitted an ellipse to the quadrilateral in an attempt to derive a smooth CME shape. A different approach to estimate the 3D CME morphology uses forward modelling assuming a graduated cylindrical shell flux rope model for the CME (Thernisien, Vourlidas, and Howard, 2009; Thernisien, 2011). This flux rope model is controlled by a few free parameters determined by fitting the flux rope with the observed CME from different viewpoints. Another method, the polarisation method, was first applied by Moran and Davila (2004). It makes use of the different anisotropy of the differential Thomson scatter cross section for different polarisations of the scattered photon. This effect allows to estimate a virtual centre of the scattered signal along each line-of-sight from the observed polarisation ratio.

Feng *et al.* (2012) developed a new mask fitting method to achieve the CME localisation and morphology. It has been used to determine the CME's propagation direction and interpret the in-situ observations from different viewpoints. The morphological evolution of the CME was analysed as well. The orientation of the neutral line in the source region was compared with the major direction of the reconstructed 3D cloud and the flux rope axis orientation from the in-situ data. To validate the newly developed reconstruction method and to seek a reliable method for the purpose of space weather prediction, in this paper the mask fitting method is compared with a few other methods which have been used to reconstruct the 3D shape. In §2 the observations of a specific CME is presented. Different methods applied to the same CME event are introduced and their corresponding results can be found in §3. In §4 we compare and combine the mask fitting method with the other four methods. The final section presents the discussions and conclusions.

Table 1. Longitude and latitude of STEREO A & B, and SOHO in Carrington coordinate system.

spacecraft	B	SOHO	A
longitude	311.49	22.86	102.21
latitude	-1.83	6.19	4.81
separation with SOHO	71.61		79.01
separation(A&B)		150.61	

**Figure 1.** The coronagraph images recorded by SECCHI/COR2 B at 21:09:05, by LASCO/C3 at 21:11:18 and by SECCHI/COR2 A at 21:08:15. The red curves outline the CME region traced by hand.

2. Observations and data reduction

The CME for which the 3D morphology is reconstructed was observed on August 7 2010. Its propagation in interplanetary space can be traced in the field of view of COR and HI in the SECCHI instrument package onboard STEREO. The CME of interest was observed as well by LASCO C2 and C3 onboard SOHO. In this paper, the 3D CME cloud is reconstructed only from Sun-centred coronagraph images. We are not dealing with the data observed by the Heliospheric Imager at this stage. The data from SECCHI/COR2 and LASCO/C3 are used. More generally, the methods introduced in the following section can be applied to any other coronagraph data if it includes polarisation measurements.

SECCHI/COR2 has a field of view extending from 2.5 to $15 R_{\odot}$, LASCO/C3 has a larger field of view extending from 3.7 to $30 R_{\odot}$. The spatial resolution of COR2 and C3 are 15 and 56 arcsec/pixel, respectively. COR2 and C3 both have a polariser which allows measurements of total, polarised and unpolarised brightness. The total time required for a polarimetric observation sequence for COR2 is around 20 s, while the corresponding observation using LASCO is around 300 s. The shorter exposure times eliminate errors arising from CME motion between exposures. All the processing of coronagraph images are done by *secchi_prep* and *lasco_prep* in SolarSoft (SSW). For a 3D reconstruction from images observed at two or three viewpoints, the positions of each spacecraft are required. In Table 1 we list the longitude and latitude of STEREO A & B,

and SOHO in the Carrington coordinate system. The separation angles between spacecraft are also mentioned.

In Figure 1 the background subtracted coronagraph images are presented. To make the CME signature more prominent, the background for COR2 is a pre-CME image recorded about 40 minutes before the eruption. Its subtraction can remove the stray light and non-CME coronal emissions. The background for C3 is a computed 12-hour minimal image centred in time at the CME eruption. Such background subtraction mainly removes the stray light and the streamer is still visible. The CME periphery was traced by hand and fitted by a parametric cubic spline. The CME-edge tie-points are indicated by red crosses for a time instance at around 21:10 UT. In our calculations we ignored the three-minute difference between the observations of COR2 A & B and C3. We have considered the interpolation of the C3 CME from two neighbouring frames in time. However, we found that the observational time of one of the neighbouring frames was almost half an hour earlier. It is very probable that the error induced by the interpolation would exceed the error from the CME propagation in three minutes. In Figure 1 shock signatures were observed which are not included in the calculations below.

The most prominent activity on the solar disk occurred at the time of the CME launch in the active region AR 11093 located at N12E31 as viewed from Earth on August 7. According to GOES light curves, a M-class flare occurred in this active region. It started around 17:55 UT and peaked at 18:24 UT. AR 11093 was visible in the east with respect to the central meridian as seen from the Earth observed by the Atmospheric Imaging Assembly (AIA; Lemen *et al.* (2012)) onboard the Solar Dynamic Observatory (SDO), whereas in the west in Extreme Ultraviolet Imager (EUVI; Wuelser *et al.* (2004)) as seen from STEREO B. It was behind the solar limb as seen from STEREO A. More details of the investigated CME and its source region can be found in Feng *et al.* (2012).

3. Descriptions and results of different 3D reconstruction methods

For direct comparisons of different reconstruction methods, all the calculations are done for the same CME event and in the same Cartesian Carrington coordinate system. X and Y axes lie in the solar equatorial plane, where X axis points to zero Carrington longitude. Z axis is the solar rotation axis.

3.1. Geometric localisation (GL)

The geometric localisation method we use resembles the work in de Koning, Pizzo, and Biesecker (2009). The reconstruction is based on the epipolar geometry (Inhester, 2006). From two viewpoints of spacecraft 1 and 2 at positions \mathbf{r}_1 and \mathbf{r}_2 , the epipolar reference axis is in the direction of $\mathbf{r}_1 \times \mathbf{r}_2$. For the stereoscopic reconstruction, all epipolar planes include the spacecraft positions \mathbf{r}_1 and \mathbf{r}_2 . The epipolar plane which also includes the Sun center is normal to the reference axis. If one certain epipolar plane is chosen, its intersection with two image planes yields two epipolar lines. In each image plane the intersection of the epipolar line with the projected CME surface produces two intersections points, one on the CME

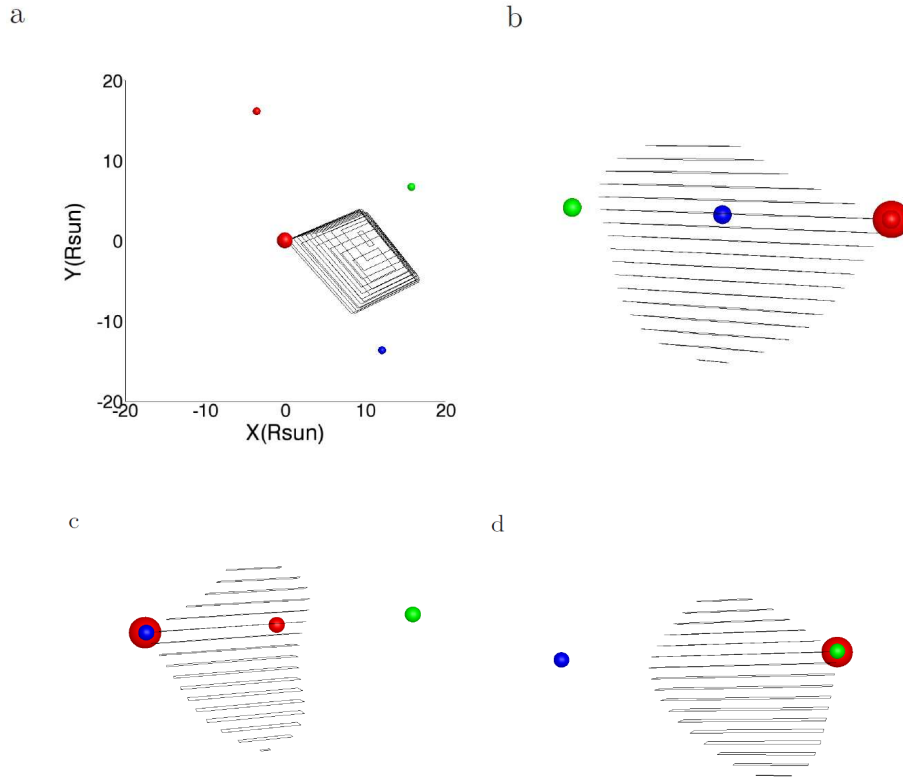


Figure 2. Reconstructed 3D CME from SECCHI/COR2 B and LASCO/C3. Panel (a) is a top view. The red sphere represents the position of the Sun. Three smaller spheres from top to bottom indicate the positions of STEREO A (red), SOHO (green) and STEREO B (blue), respectively. Their distances to the Sun are scaled. Panel (b) to (d) are the reconstructed 3D CME as seen by STEREO A, STEREO B, and SOHO.

leading edge and the other on the rear edge. The back projections of these four points form one quadrilateral in each epipolar plane which contains the CME. The stacked set of quadrilaterals on different epipolar planes yields a volume which to a first approximation reconstructs the CME shape in 3D space.

As an example, we present in Figure 2 the reconstruction that resulted from only two views, SECCHI/COR2 B and LASCO/C3. Panel (a) is a view of the 3D CME from a vantage point above the north pole. From this particular viewpoint, the position of the 3D CME relative to the three view directions from STEREO A, B and SOHO can be easily disentangled. For a low-latitude CME around the ecliptic plane, as the case in this paper, this information is very helpful to tell whether a CME arrives at the Earth or at another planet/spacecraft. A high-latitude CME may eventually deflect to the heliospheric current sheet close to the ecliptic plane where planets reside, e.g. Zuccarello *et al.* (2012) and Shen *et al.* (2011). Panel (b) to (d) are the projections of the reconstructed CME onto the image plane of STEREO A & B and SOHO. They have very similar

shape to the CME observed by COR2 A and LASCO C3. However, the CME shape in Panel (b) and in Figure 1 as seen from STEREO A do not fit each other exactly. Since the reconstruction only includes the CME periphery from COR2 B and C3, it is not surprising that we arrive at this result. The deviations reveal that observations from a third viewpoint will further constrain the CME shape.

In Figure 3, the red quadrilateral is the reconstruction from COR2 A and B in the epipolar plane across the solar centre. The green and blue quadrilaterals are similar to the red one, whereas constrained by COR2 A and C3, COR2 B and C3, respectively. Because three spacecraft were almost positioned in the same plane, these three epipolar planes (three quadrilaterals) determined by STEREO A, B, SOHO, and the Sun are roughly coplanar.

It is obvious that the red quadrilateral extends in a much bigger range in longitude than the green and blue ones. In another word, its corresponding uncertainty of reconstruction is much larger. Pizzo and Biesecker (2004) investigated the uncertainty of the 3D reconstructions with the geometric localisation technique as a function of the separation angle. Synthetic white-light image pair simulating STEREO-like coronagraph observation of a modeled 3D CME were created. The reconstructions from the synthetic image pair at different separation angles and the modeled 3D CME were compared. The ratio of the area of the reconstructed quadrilateral to the actual area was around unity at a 90-degree separation, and increased almost monotonically to both 0 and 180-degree separations. In Figure 3, the reconstructions in red has an area much larger than the green and blue one due to the large separation angle between STEREO A and B. This is consistent with the scenario depicted in Pizzo and Biesecker (2004).

Another immediate result which can be derived from Figure 3 is that the common polygon area which results from the intersection of the red, green and blue quadrilaterals is more constraining than any of the individual quadrilaterals from just two view directions. We therefore strongly recommend that the third viewpoint should be included, if the data is available.

However, as mentioned in the beginning of this section, an epipolar plane depends on the position of the two observing spacecraft. If more than two spacecraft are used, epipolar planes still need to be constructed between each pair of spacecraft and epipolar planes from different spacecraft pairs in general will not match. However, if three spacecraft are located in a common plane with the Sun centre, the various epipolar planes can be approximated by planes parallel to the common spacecraft plane. This is equivalent to assuming an affine instead of a projective viewing geometry. The error introduced is small $\tilde{O}(r_{CME}/r_{spacecraft})$ as long as the CME is observed close to the Sun, where the distance r is measured from the Sun. If the three spacecraft do not lie in a common plane the reconstruction by geometric localisation is still possible, but more complicated, because it cannot be reduced any more to a set of planar intersections. Instead the CME volume for each pair of spacecraft could be determined as a set of quadrilaterals on stacked epipolar planes and the intersections must be calculated from these volumes as a whole rather than from the quadrilaterals in each (approximate) epipolar plane.

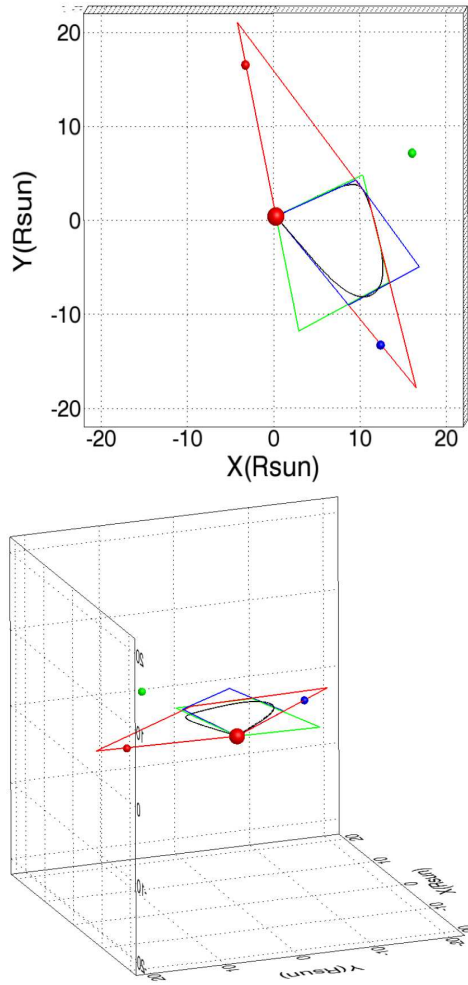


Figure 3. Geometric localisation of the CME in the epipolar plane containing the solar centre from STEREO A & B in red, from STEREO A and SOHO in green and from STEREO B and SOHO in blue. The black curve is the reconstruction in the solar equatorial plane from the mask fitting method in the next subsection. The red sphere represents the Sun. Three smaller spheres are STEREO A, SOHO and STEREO B. The color code of the three spacecraft is the same as in Fig. 2. Upper: a top view of the reconstructions; Bottom: a side view showing the small deviation of the epipolar planes from the equatorial plane.

3.2. Mask fitting (MF)

The mask fitting method geometrically follows up the previous concept, however, instead of performing back-projections and finding intersections on epipolar planes, we use forward-projections from a discretised 3D space to verify whether a 3D point is potentially inside or outside the CME volume. Using this concept, the epipolar geometry is not required explicitly. The details of this method are described in Feng *et al.* (2012).

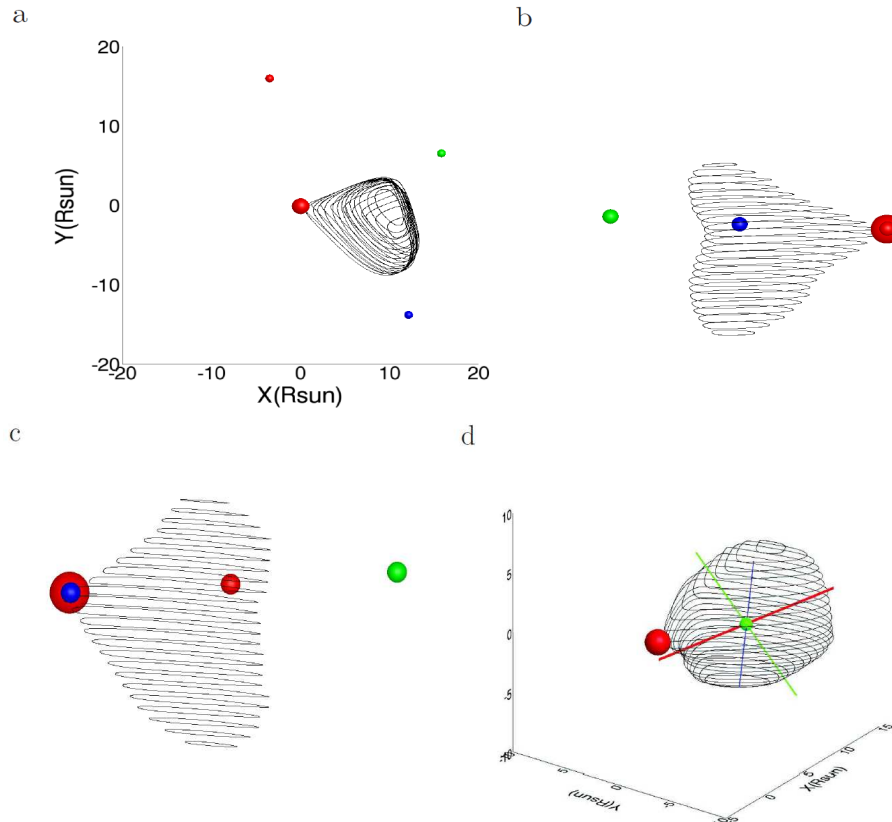


Figure 4. Reconstructed 3D CME with the mask fitting method from SECCHI/COR2 B and LASCO/C3. Panel (a) is a top view. The red sphere localise the position of the Sun. Three smaller spheres are STEREO A, SOHO and STEREO B. The color code of the three spacecraft is the same as in Fig. 2. Panel (b) and (c) are the reconstructed 3D CME as seen by STEREO A, STEREO B. In panel (d) the 3D CME and its three principle axes are plotted. The three axes in red, green and blue are the major, intermediate and minor axes, respectively. The small green sphere represents the geometric centre of CME.

As a first step, three CME masks are created according to Figure 1. Pixel value is one inside the CME periphery and zero outside. Then we discretise a 3D cube centred at the Sun and in the range from $-15 R_{\odot}$ to $15 R_{\odot}$ for all three coordinate axes. Each point in this 3D cube is projected onto three image planes of STEREO A & B and SOHO, respectively. Only those points which project into the masks of all three images are considered to be the 3D points belonging to the CME. Afterwards, Bézier curves are employed to smooth the boundary of the resulting polygonal volume. In Figure 3 the black curve shows a slice of the smoothed reconstructed CME volume in the solar equatorial plane $z=0$.

The different views of the reconstructed 3D CME with the mask fitting method can be found in Figure 4. Compared with the results obtained by using epipolar geometry explicitly with STEREO/COR B and LASCO data, the reconstruction from three views provides a better solution, which can be

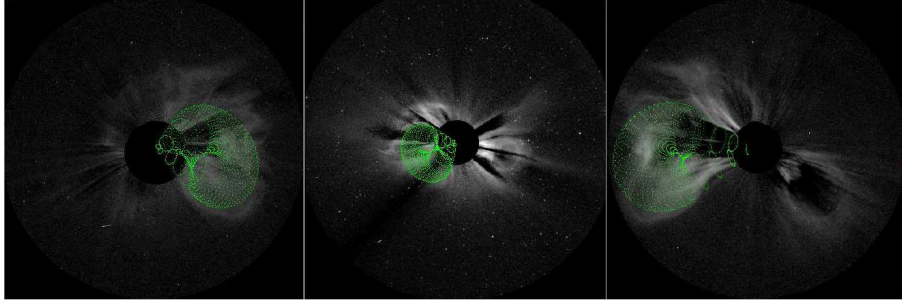


Figure 5. Fitting of a flux rope to the CME observed by COR2 A, C3 and COR2 B with the GCS forward modeling method.

verified by panel (b). The heart-like shape along the CME leading edge as seen from STEREO A is now clearly visible, whereas this feature is not present in panel (b) of Figure 2. In panel (d) three principle axes and geometric centre of the 3D CME volume are shown. Details of computation can be found in Feng *et al.* (2012). Note that the geometric centre might not be the centre of gravity since a uniform density distribution was assumed. In this paper we use it as an approximation of the centre of gravity to make comparisons with other methods.

3.3. GCS forward modeling (FM)

Thernisien, Howard, and Vourlidas (2006) and Thernisien, Vourlidas, and Howard (2009) developed a forward-modeling technique for flux-rope-like CMEs using an empirically defined model of a flux rope, the graduated cylindrical shell (GCS). It consists of a tubular section forming the main body of the structure attached to two cones that correspond to the legs of the CMEs. The parameters constraining the shape of the flux rope are determined by visual comparison of the projected 3D flux rope to observations. The optimisation is achieved by trial and error. One hour after launch, the CME leading front became concavely deformed and its shape can no longer match that of a single flux rope. Even though a flux rope does a poor job for this CME, as a first estimate of the 3D propagation direction and the spatial extension of the CME, in Figure 5 a flux rope is fitted to the observed CME from three viewpoints, i.e. STEREO B, LASCO and STEREO A. We followed the proposal of Thernisien, Vourlidas, and Howard (2009) and fitted two flux ropes to the observations from three viewpoints. The results are presented in Figure 6 in blue color together with a single flux rope in red for comparison.

3.4. Polarisation ratio technique (PR)

The polarisation ratio technique was first applied to SOHO/LASCO coronagraph images before the launch of STEREO (Moran and Davila, 2004; Dere, Wang, and Howard, 2005). Theoretically, the degree of polarisation of Thomson-scattered light by electrons in the corona is a sensitive function of the scattering angle between the direction

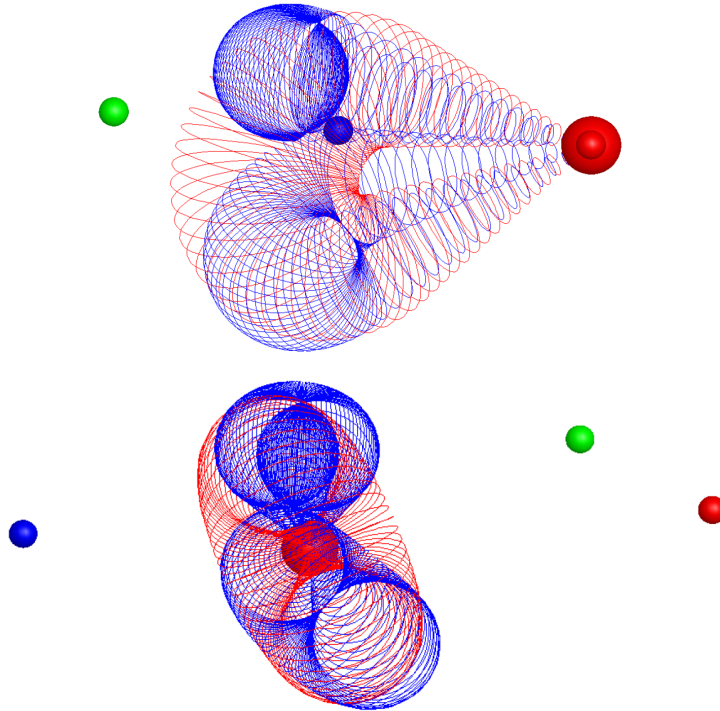


Figure 6. 3D flux ropes with the best-fit parameters derived from the forward modeling method. The red flux rope represents one single flux rope fitted to the CME observed from three viewpoints. Two blue flux ropes are combined together to fit to the observed CME. The red sphere stands for the Sun and three smaller spheres indicate the directions to three spacecraft. The same color code as in Fig. 2 applies here to the three spacecraft. Top: flux ropes as seen from STEREO A. Bottom: flux ropes as seen from the top of the fitted single flux rope.

of the incident light and the direction towards the observer (Billings, 1966). Hence the ratio of the polarised brightness pB to the unpolarised brightness $tB - pB$, where tB is the total brightness, is also a function of the scattering angle. Equivalently, this angle can be converted to an effective distance of the scatterer from the plane of the sky (POS). Observationally, the polarisation ratio can be retrieved from the polarimetric observation sequence by LASCO or COR2 for each pixel within the CME region. Comparing with the theoretical relation, we can derive a weighted distance of the centre of scattering along the line-of-sight for each pixel. Mierla *et al.* (2009) applied this technique to several CMEs observed by SECCHI/COR A & B independently, and derived the distribution of LOS scattering centres of the CME. Moran, Davila, and Thompson (2010) has validated this method through triangulation. De Koning and Pizzo (2011) have suggested that this method can be used in space weather forecasting.

In order to remove the contributions (F-corona, stray-light, streamer contribution) other than the CME feature itself, a pre-event image was subtracted. The emission in the coronagraph images is Thomson scattered light, but in some

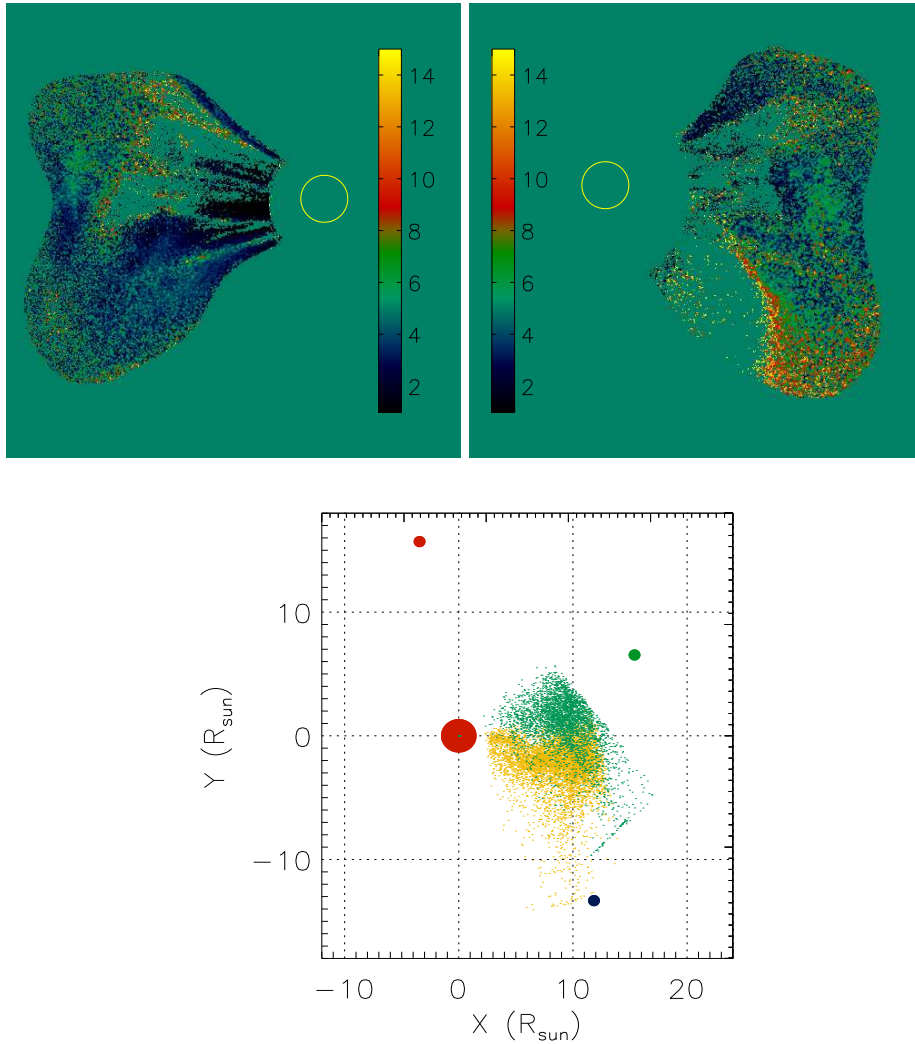


Figure 7. Reconstructed 3D points from the polarisation ratio method. Top panels: the weighted distance of each pixel in the CME region to the respective POS calculated from COR2 A (left) and COR2 B (right). The color bar scales the distance in units of solar radius. The yellow circle mark the position of the solar disk. Bottom panel: A top view of the reconstructed 3D points. To make the dot density visible, we plotted the scattering centre every 50 points for all the 3D points. The yellow points are from the reconstruction from COR2 A, and the green points from COR2 B. The red sphere indicates the Sun, and three smaller ones mark the direction to three spacecraft. The color code of the three spacecraft is the same as in Fig. 2.

situations also Halpha emission can be observed (see e.g. Mierla *et al.* (2011)). If we assume that only Thomson scattered light was observed, then we could use the PR method to derive the 3D location of the CME. In order to increase the signal-to-noise ratio, the frames with the CME were smoothed by using a 5-pixel-by-5-pixel median filter. The size along LOS is restricted to 15 solar radii (in front and behind the POS), and the step along LOS is every 0.001 solar radii. The pixels where the intensity was smaller than 5% of the CME region mean value were not included in calculation. This was done in order to reduce artifacts in the 3D reconstruction.

Fig. 7 shows the results of applying the PR method to the data of COR2 A and B on the left and right panel, respectively. The color bar indicates the distances in solar radii of the scattering centres off the POS obtained for each image pixel inside the CME projection. The bottom panel is a top view of the reconstructed 3D points. Yellow and green points represent the results from COR2 A and B, respectively. As the PR method can only determine an absolute distance to the POS, an ambiguity of two symmetric solutions arises. In cases that the CME source region is known, its position in the solar disk can be utilised as a reference. From the close time of flare eruption and CME ejection, the source region is very probably the AR 11093. It was located on the western hemisphere as seen from the STEREO B. From STEREO A, it is not visible in front of the solar limb. Therefore, we assume that all the reconstructed points from the PR method are behind the POS as seen from STEREO A, whereas they are in front of the POS as seen from STEREO B.

Comparing the results from COR2 A and B in Figure 7, we found that in general they are consistent with each other. In the bottom panel of the top view, substantial part of the yellow and green points overlap. However, the misalignment is also obvious. The longitude of the centre of gravity differs by 19.4 degrees. In addition, the reconstruction from COR2 B in the top panels indicates that the southern part has a larger distance to the POS than the northern part, while the reconstruction from COR2 A does not show this trend. We partly attributed the misalignment to the fact that some features can only be seen by one instrument. In addition, in the above reconstructions, we assumed that the CME is fully behind the solar limb as seen from STEREO A and fully in front of the solar limb as seen from STEREO B. In reality, this may not be true for all pixels.

We note that two symmetric solutions exist for one pixel, i.e., one in front of the POS and the other behind. This ambiguity can be partly disentangled by the identification of the source region in EUV images or by the best match of stereoscopic observations. However, CME source regions are not always apparent. e.g., for stealth CMEs (Robbrecht, Patsourakos, and Vourlidas, 2009). Furthermore, without the information of the density distribution along the line of sight, the determined distance to POS might contain some errors (Mierla *et al.*, 2009) even if we include the stereoscopic results. A further source of error of the polarisation ratio method may be that low temperature chromospheric material might enter the coronagraph field of view whose radiation mechanism is totally different from the Thomson scattering. Therefore, in those cases the polarisation ratio technique does not work properly (Mierla *et al.*, 2011).

3.5. Local correlation tracking plus triangulation (LCT-TR)

A crucial step in this approach is to correlate the CME texture in both images before the triangulation. Since a CME often appears as a diffuse cloud, instead of the feature-based approach Mierla *et al.* (2009) applied a local correlation tracking (LCT) method to find corresponding points in a STEREO image pair. In this method, we first co-aligned the images in STEREO mission plane such that the epipolar lines become nearly horizontal. The elements to be matched are small subimages of a fixed size, called match windows. The criterion which decides whether two such windows in different images are positioned on the same object is the magnitude of their mutual correlation coefficient. The cross correlation is calculated from windows on two STEREO images on a common epipolar line. For a given position of one window on the epipolar line in one image, the corresponding position of the matching window in the other image is determined by the correlation maximum.

Once the correspondence between pixels is established, the point in 3D space is calculated through back projection (Inhester, 2006). In Figure 8, we present the LCT-TR reconstruction of the CME from COR2 data. A threshold of acceptance for the calculated correlation minimum of 0.7 was used in Figure 8. In order to find correlations in two images, the match window (11x11 pixels) was fixed in a position on a given epipolar line in one image and move it along the same epipolar line in the other image. The search window was 512 pixels on the horizontal direction. As the CME was observed at the opposite limb in the two images, the search for corresponding features was flipped such that, for a pixel on the left side of image A, the search window was located on the right side of image B. The upper panel is a top view. The reconstructed CME shows a propagation direction towards SOHO which was, however, not validated by the in-situ observation close to the Earth (Feng *et al.*, 2012). It may be that the lower acceptance limit of 0.7 for the correlation was chosen too small causing a significant number of false correlations to be passed. A higher value of the correlation limit, however, would have reduced the number of correlations markedly. The lower panel is a view from STEREO B. We found that most of the points within the CME periphery have a correlation coefficient less than 0.7. The results of LCT-TR clearly show a poor performance when the separation angle of two STEREO spacecraft is large.

4. Comparison and Combination of different methods

4.1. Geometric localisation and mask fitting

The reconstruction of the CME morphology is a typical inverse process problem. The geometric localisation method applies back projection to find a solution whereas we use forward projections in the mask fitting algorithm. In Figure 3, we can see that the black curve from the mask fitting method fits the pentagon from the geometric localisation quite well. The small difference between the mask fitting and geometric localization is that the epipolar plane does not necessarily lie on the solar equatorial plane of $z = 0$. They deviate with each other by a few

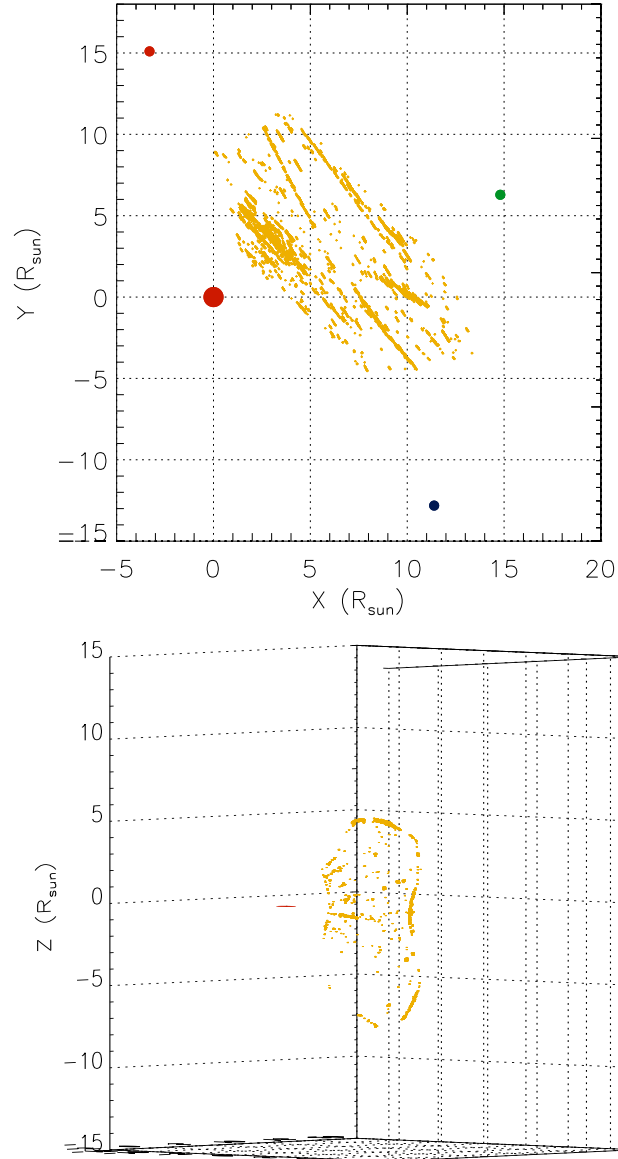


Figure 8. Top panel: A top view of the reconstruction with the LCT-TR method from COR 2 A & B. The four spheres have the same meaning as Figure 7. Bottom panel: a view from STEREO B. In both panels, the lower limit of the correlation coefficient is set to 0.7 for the correspondence.

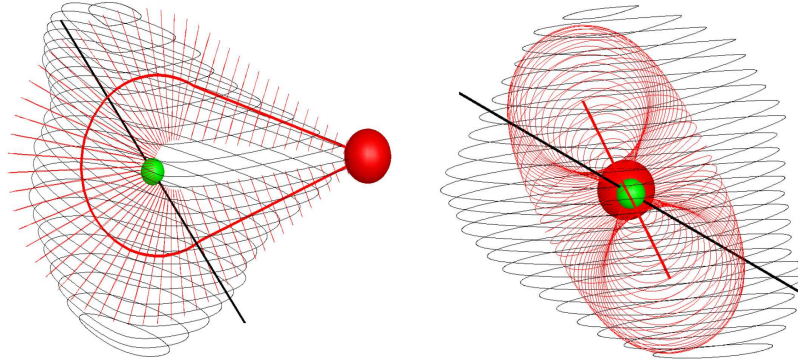


Figure 9. Comparison of the single flux rope from forward modeling in red with the results from mask fitting method in black. The red sphere is the Sun. The red curve is the CME skeleton from the GCS model. The black straight line indicates the major principle axis of the 3D CME cloud derived with the mask fitting method. The front view of the flux rope is presented in the left panel. The top view of the flux rope is in the right panel.

degrees as indicated in the bottom panel of Figure 3. Nevertheless, from Figure 3 we expect that in principle these two methods produce consistent results.

Geometric localisation suffers from the limitation that the epipolar plane is uniquely determined by the positions of the two spacecraft and the point to be reconstructed. Only in the rare case that the third spacecraft also lies in this epipolar plane the constraints from the three viewpoints can be combined in a simple way. The mask fitting method, on the other hand, can integrate the data from an unlimited number of viewpoints with arbitrary positions. Obviously, the more view positions are included in the reconstructions, the more constrained and reliable is the result.

4.2. GCS forward modeling and mask fitting

As already stated in §3.3, when a CME does not have the shape of a flux rope, the GCS forward modeling method can only provide an approximation of the 3D CME morphology. It is the common feature for any forward modeling that the result strongly depends on an a-priori geometrical assumption. However, real CMEs are not always close to a flux-rope-like shape. Therefore, we found that the mask fitting method has more flexibility than the forward modeling method. In the left panel of Figure 9, the fitted flux rope and the 3D CME reconstructed from the mask fitting method are shown superposed along a view direction which is perpendicular to the plane of the flux rope skeleton. We can see how much the single idealised flux rope may deviate from the true CME.

Both the orientation of the flux rope characterised by the tilt angle γ in Thernisien, Howard, and Vourlidas (2006) and the major principle axis from the mask fitting method are in the northeast-southwest direction as can be seen in the right panel of Figure 9. The difference of the projection of the major principle axis from the tilt angle from GCS model is about 30 degrees.

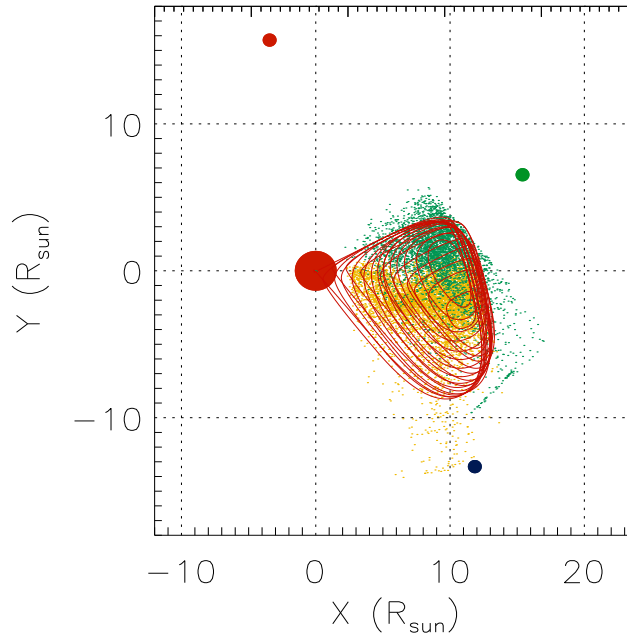


Figure 10. The top view of the 3D CME reconstructed with the MF technique in red color, and with the PR method from COR2 A & B in yellow and green, respectively.

4.3. Polarisation ratio and mask fitting

The polarisation ratio method has the advantage that only the data from one viewpoint and some additional information like the location of the CME source region is required for a unique reconstruction. It yields some limited information also about the CME's interior structure. However, the polarisation ratio can only provide the depth of a virtual scattering centre for each LOS but not the depth range over which the CME extends along the LOS. Figure 10 shows an overplot of the reconstructions with the polarisation ratio and mask fitting methods. Apparently, the MF method locates the CME mostly in the overlap region of the results with the PR method from COR2 A and B images.

Concerning the ambiguity of the two symmetric solutions from the PR method in § 3.4, we have resolved this ambiguity by reference to the location of the CME source region. In cases where the knowledge of the source region is not available, the CME shape, reconstructed with the MF method could also be used as reference. For the CME studied here, the MF result suggests that the CME centre is completely in front of the POS as seen from STEREO B and behind the POS for most pixels of STEREO A. We therefore selected this respective solution for the PR method. We note that there is some probability on lines-of-sight from STEREO A passing close to the Sun that the PR scattering centre lies in front of the respective POS. Since the MF method gives only the shape but

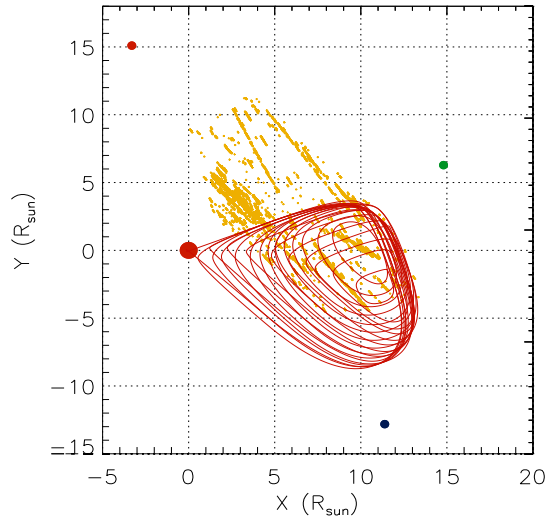


Figure 11. The comparison of the 3D CME reconstructed from MF and LCT-TR methods. The results are shown in red and yellow, respectively.

no density distribution inside the CME volume, predictions about the scattering centre must be treated with care if the MF volume extends to both sides of the POS. In addition, we found that the centres of gravity obtained with MF and PR A are quite close, however, those derived from MF and PR B differ by more than one solar radius. Similarly, De Koning and Pizzo (2011) combined the 3D CME reconstructed with geometric localisation method from two viewpoints to resolve the PR ambiguity.

4.4. Local correlation tracking plus triangulation and mask fitting

LCT-TR method works well for small separation angles (Mierla *et al.*, 2009). When the separation angle increases, the capability of LCT in solving the correspondence problem decreases. In Figure 11 a top view of the reconstructed CME with the MF and LCT-TR methods are indicated in red and yellow, respectively. We found a large discrepancy between them. The 3D CME location derived from the LCT-TR method indicates a propagation of the CME towards the Earth, whereas the CME position obtained with the MF method is consistent with a propagation towards the Venus (Feng *et al.*, 2012). As already pointed out in §3.5, the in-situ measurements around the Earth did not detect any ICME related signature. However, the Venus Express spacecraft detected the shock and ICME arrival (Feng *et al.*, 2012). Therefore, we take this as an evidence that the MF method for large spacecraft separation angles yields a more reliable 3D reconstruction than the LCT-TR method. The LCT-TR method appears to fit quite nicely inside the red quadrilateral obtained from geometric localisation. In other words, LCT-TR suffers from the same large-angle separation problem that two-spacecraft geometric localisation does.

5. Discussion and Conclusions

In this study we made a comprehensive comparison of reconstruction results between five different methods, which can produce the morphological shape of the 3D CME. The corresponding results and their comparisons with the newly developed mask fitting method are presented as well. For a quantitative comparison, we compiled in Table 2 the centre of gravity of the various 3D reconstructions and their range in longitude and latitude. From the fourth column of the table, we list the maximum and minimum of longitude and latitude of the reconstructed 3D CME points.

For the geometric localisation method, we have already found in §4.1 that its result is consistent with the results obtained with mask fitting method. Therefore, we present the longitude and latitude information for both methods in the same row in Table 2. For the forward modeling method, the centre of gravity is obtained by assuming that the mass distribution has the same formula as in Thernisien, Howard, and Vourlidas (2006). As it is a symmetric distribution, we expect that the centre of gravity lies in the axis of symmetry of the modeled flux rope. Hence the centre of gravity has the same longitude and latitude as the source region central position. We found that the numerically calculated latitude and longitude widths of the fitted flux rope model is consistent with the values analytically given by Equation (1) and (2) in Rodriguez *et al.* (2011). For a single GCS flux rope, the analytical formula gives a longitude range of about 45 degrees and a latitude range of about 69 degrees. From Table 2, these two figures which were calculated numerically are 46.6 and 69.6 degrees, respectively.

An inspection of the longitude and latitude of the center of gravity indicates that MF/GL, FM and PR A result in similar values. The difference in longitude is not larger than 1.3 degrees, and in latitude is within 0.6 degrees. PR B shows a similar latitude, however, the longitude deviates about 19 degrees. Even larger deviations from those of the MF/GL methods were obtained with the LCT-TR method, both in longitude and latitude.

Concerning the spatial extension of the CME in 3D, the results in Table 2 are not fully consistent with each other. For the FM method, a single flux rope inclined in the NE-SW direction is fitted to coronagraph images observed from three viewpoints. As mentioned in §3.3, the observed CME was strongly deformed away from a flux rope. It is not surprising that forward modeling method has a different longitude and latitude extension than the mask fitting method. Comparing with the MF method, we found a smaller longitude range for the FM results. The latitude range derived from both methods agrees well. Interestingly, the longitude range from the MF method happens to be in general consistent with the range of the overlap of the PR A and PR B results. There is a similar trend for the latitude minimum. However, the latitude maximum of PR methods are 14 degrees higher. The longitude and latitude range derived from the LCT-TR method shows a much bigger deviation from the other four methods. In cases of large separation angle, LCT-TR method does a poor job for the 3D reconstruction of CMEs.

In summary, for the event on August 7, we found that the mask fitting method achieves the same precision for the CME's 3D morphology as the geometric

Table 2. Longitude, latitude of the centre of gravity, and longitude, latitude ranges of the reconstructed 3D CME with mask fitting/geometric localisation, forward modeling, polarisation ratio and local correlation tracking plus triangulation methods. The Carrington coordinate system is used. All the values are in units of degrees.

Method	lon.	lat.	lon. min	lon. max	lat. min	lat. max
MF/GL	-13.3	-7.7	-48.0	24.7	-42.5	25.3
FM ¹	-13.4	-7.3	-35.6	11.0	-42.0	27.6
PR A	-14.6	-7.9	-70.3	15.6	-42.1	39.1
PR B	4.8	-6.8	-40.3	41.7	-55.6	42.8
LCT-TR	27.8	2.8	-29.7	89.4	-39.2	39.2

¹derived from the fit of a single flux rope

localisation method when the data from the same number of viewpoints are used. Compared with the forward modeling method, mask fitting is more flexible, no a-priori geometrical assumption is required. We found that the mask fitting method can be utilised to remove the ambiguity in the polarisation ratio method. In addition, the reconstructed CME with the mask fitting method localises almost in the overlap region derived with the polarisation ratio method from COR2 A and B. We did not find a consistent result of the local correlation tracking plus triangulation with the other four methods.

In general, the mask fitting method produces a good 3D reconstruction of the CME surface if the data from three spacecraft with sufficient angular separation is used. However, we are lacking the detailed internal structure within the CME volume. In future, we will explore the MF method for the surface reconstruction in combination with tomography to resolve the internal density distribution. The localisation of the CME relative to the plane of the sky is helpful to estimate the CME mass from coronagraph images, e.g., Colaninno and Vourlidis (2009). It can be compared to the mass calculation from other observations, e.g., Aschwanden *et al.* (2009) and Tian *et al.* (2012). We anticipate that with the information of the known propagation direction, spatial extension and density distribution of a CME, a more precise prediction of space weather can be made.

Acknowledgements We thank S. Gissot for providing the LCT program. STEREO is a project of NASA. The SECCHI data used here were produced by an international consortium of the Naval Research Laboratory (USA), Lockheed Martin Solar and Astrophysics Lab (USA), NASA Goddard Space Flight Center (USA), Rutherford Appleton Laboratory (UK), University of Birmingham (UK), Max-Planck-Institut for Solar System Research (Germany), Centre Spatiale de Liège (Belgium), Institut d’Optique Théorique et Appliquée (France), Institut d’Astrophysique Spatiale (France). LF is supported by National NSFC under grant 11003047 and by MSTC Program 2011CB811402. LF also acknowledges the Key Laboratory of Dark Matter and Space Astronomy, CAS, for financial support. The contribution of BI benefitted from support of the German Space Agency DLR and the German ministry of economy and technology under contract 50 OC 0904. MM thanks MPS for financial support. Part of her work was

also supported from the project TE 73/11.08.2010. The work at the MPS was supported by DLR contract 50 OC 0904.

References

- Berger, M.A., Field, G.B.: 1984, *J. Fluid. Mech.* **147**, 133.
- Aschwanden, M.J., Nitta, N.V., Wuelser, J.-P., Lemen, J.R., Sandman, A., Vourlidas, A., and Colaninno, R.C.: 2009, *Astrophys. J.* **706**, 376.
- Billings, D.E.: 1966, *New York: Academic Press, —c1966*.
- Brueckner, G.E., Howard, R.A., Koomen, M.J., Korendyke, C.M., Michels, D.J., Moses, J.D., Socker, D.G., Dere, K.P., Lamy, P.L., Llebaria, A., Bout, M.V., Schwenn, R., Simnett, G.M., Bedford, D.K., and Eyles, C.J.: 1995, *Solar Phys.* **162**, 357.
- Byrne, J.P., Maloney, S.A., McAteer, R.T.J., Refojo, J.M., and Gallagher, P.T.: 2010, *Nature Communications* **1**.
- Colaninno, R.C. and Vourlidas, A.: 2009, *Astrophys. J.* **698**, 852.
- de Koning, C.A., Pizzo, V.J., and Biesecker, D.A.: 2009, *Solar Phys.* **256**, 167.
- de Koning, C.A. and Pizzo, V.J.: 2011, *Space Weather* **9**, 3001.
- Dere, K.P., Wang, D., and Howard, R.: 2005, *Astrophys. J.* **620**, L119.
- Domingo, V., Fleck, B., and Poland, A.I.: 1995, *Solar Phys.* **162**, 1.
- Feng, L., Inhester, B., Wei, Y., Gan, W.Q., Zhang, T.L., and Wang, M.Y.: 2012, *Astrophys. J.* **751**, 18.
- Howard, R.A., Moses, J.D., Vourlidas, A., Newmark, J.S., Socker, D.G., Plunkett, S.P., Korendyke, C.M., Cook, J.W., Hurley, A., Davila, J.M., Thompson, W.T., St Cyr, O.C., Mentzell, E., Mehalick, K., Lemen, J.R., Wuelser, J.P., Duncan, D.W., Tarbell, T.D., Wolfson, C.J., Moore, A., Harrison, R.A., Waltham, N.R., Lang, J., Davis, C.J., Eyles, C.J., Mapson-Menard, H., Simnett, G.M., Halain, J.P., Defise, J.M., Mazy, E., Rochus, P., Mercier, R., Ravet, M.F., Delmotte, F., Auchere, F., Delaboudiniere, J.P., Bothmer, V., Deutsch, W., Wang, D., Rich, N., Cooper, S., Stephens, V., Maahs, G., Baugh, R., McMullin, D., and Carter, T.: 2008, *Space Science Reviews* **136**, 67.
- Inhester, B.: 2006, *ArXiv Astrophysics e-prints*, arXiv:astro-ph/0612649.
- Kaiser, M.L., Kucera, T.A., Davila, J.M., St. Cyr, O.C., Guhathakurta, M., and Christian, E.: 2008, *Space Science Reviews* **136**, 5.
- Lemen, J.R., Title, A.M., Akin, D.J., Boerner, P.F., Chou, C., Drake, J.F., Duncan, D.W., Edwards, C.G., Friedlaender, F.M., Heyman, G.F., Hurlburt, N.E., Katz, N.L., Kushner, G.D., Levay, M., Lindgren, R.W., Mathur, D.P., McFeaters, E.L., Mitchell, S., Rehse, R.A., Schrijver, C.J., Springer, L.A., Stern, R.A., Tarbell, T.D., Wuelser, J.-P., Wolfson, C.J., Yanari, C., Bookbinder, J.A., Cheimets, P.N., Caldwell, D., Deluca, E.E., Gates, R., Golub, L., Park, S., Podgorski, W.A., Bush, R.I., Scherrer, P.H., Gummin, M.A., Smith, P., Auken, G., Jerram, P., Pool, P., Soufli, R., Windt, D.L., Beardsley, S., Clapp, M., Lang, J., and Waltham, N.: 2012, *Solar Phys.* **275**, 17.
- Mierla, M., Inhester, B., Marqué, C., Rodriguez, L., Gissot, S., Zhukov, A.N., Berghmans, D., and Davila, J.: 2009, *Solar Phys.* **259**, 123.
- Mierla, M., Inhester, B., Antunes, A., Boursier, Y., Byrne, J.P., Colaninno, R., Davila, J., de Koning, C.A., Gallagher, P.T., Gissot, S., Howard, R.A., Howard, T.A., Kramar, M., Lamy, P., Liewer, P.C., Maloney, S., Marqué, C., McAteer, R.T.J., Moran, T., Rodriguez, L., Srivastava, N., St. Cyr, O.C., Stenborg, G., Temmer, M., Thernisien, A., Vourlidas, A., West, M.J., Wood, B.E., and Zhukov, A.N.: 2010, *Annales Geophysicae* **28**, 203.
- Mierla, M., Chifu, I., Inhester, B., Rodriguez, L., and Zhukov, A.: 2011, *Astron. Astroph.* **530**, L1.
- Moran, T.G. and Davila, J.M.: 2004, *Science* **305**, 66.
- Moran, T.G., Davila, J.M., and Thompson, W.T.: 2010, *Astrophys. J.* **712**, 453.
- Pizzo, V.J. and Biesecker, D.A.: 2004, *Geophys. Res. Lett.* **31**, 21802.
- Robbrecht, E., Patsourakos, S., and Vourlidas, A.: 2009, *Astrophys. J.* **701**, 283.
- Rodriguez, L., Mierla, M., Zhukov, A.N., West, M., and Kilpua, E.: 2011, *Solar Phys.* **270**, 561.
- Shen, C., Wang, Y., Gui, B., Ye, P., and Wang, S.: 2011, *Solar Phys.* **269**, 389.
- Thernisien, A.F.R., Howard, R.A., and Vourlidas, A.: 2006, *Astrophys. J.* **652**, 763.
- Thernisien, A., Vourlidas, A., and Howard, R.A.: 2009, *Solar Phys.* **256**, 111.

- Thernisien, A.: 2011, *The Astrophysical Journal Supplement Series* **194**, 33.
- Thernisien, A., Vourlidas, A., and Howard, R.A.: 2011, *Journal of Atmospheric and Solar-Terrestrial Physics* **73**, 1156.
- Tian, H., McIntosh, S.W., Xia, L., He, J., and Wang, X.: 2012, *Astrophys. J.* **748**, 106.
- Wueller, J.-P., Lemen, J.R., Tarbell, T.D., Wolfson, C.J., Cannon, J.C., Carpenter, B.A., Duncan, D.W., Gradwohl, G.S., Meyer, S.B., Moore, A.S., Navarro, R.L., Pearson, J.D., Rossi, G.R., Springer, L.A., Howard, R.A., Moses, J.D., Newmark, J.S., Delaboudiniere, J.-P., Artzner, G.E., Auchere, F., Bougnet, M., Bouyries, P., Bridou, F., Clotaire, J.-Y., Colas, G., Delmotte, F., Jerome, A., Lamare, M., Mercier, R., Mullet, M., Ravet, M.-F., Song, X., Bothmer, V., and Deutsch, W.: 2004, *Society of Photo-Optical Instrumentation Engineers (SPIE) Conference Series* **5171**, 111.
- Zuccarello, F.P., Bemporad, A., Jacobs, C., Mierla, M., Poedts, S., and Zuccarello, F.: 2012, *Astrophys. J.* **744**, 66.

